Proceedings of the
Annual Stability Conference
Structural Stability Research Council
Charlotte, North Carolina, April 11-14, 2023

Stability and design of stainless WF shapes in combined compression and bending

Anne-Sophie Gagné[1], Liya Li[2], Nicolas Boissonnade[3]

Abstract
Stainless steel is characterized by a non-linear material response, which, unlike regular carbon steel, does not exhibit a typical yield plateau. This is sufficient to invalidate the classical design rules used in steel construction. This paper therefore proposes a different approach to predict the resistance of stainless steel open cross-sections. First, numerical models suited to stainless steel sections are developed and validated against experimental results. The models are then used to perform finite element simulations allowing to consider many stainless steel grades, load cases and geometries. The numerical reference results may then be used to assess the merits of a two-stage approach for simple load cases: an approach based on strains for compact sections, and an approach based on local buckling curves for more slender sections. Further, an interaction equation is calibrated for combined load cases. The proposed design approach is shown economical, simple and safe, as well as being an improvement over the performance of existing approaches.

1. Introduction
The present paper relates to predicting the cross-sectional resistance of stainless steel wide flange shapes submitted to compression, bending, or a combination of compression and bi-axial bending; our focus is on I-shaped stainless steel sections fabricated by laser welding. Although less frequently used than carbon steel, stainless steel is increasingly used in structural applications due to (i) its high resistance to corrosion and fire, (ii) great ductility, (iii) aesthetics and (iv) ease of maintenance. The material response of stainless steel is quite different from carbon steel and its so-called "plastic plateau", as stainless steel provides an entirely non-linear stress-strain response with important strain hardening reserves. Consequently, this invalidates most current design rules which typically assume plastic stress distributions, i.e., the presence of a plastic plateau.

Therefore, stainless steel design shall involve specific, dedicated design recommendations that not only reflect the real material response but also exploit strain hardening reserves adequately. Various standards (AISC 2013; EN1993-1-4 2006) propose explicit sets of design rules for stainless steel members, which can be shown to fail satisfying these requirements. Recently, the

[1] MSc student, Laval University, <anne-sophie.gagne.2@ulaval.ca>
[2] Post-Doc student, Laval University, <liya.li.1@ulaval.ca>
[3] Professor, Laval University, <nicolas.boissonnade@gci.ulaval.ca>

resistance to compression and/or to bending of stainless steel open sections has gained attention, namely through the development of the so-called Continuous Strength Method C.S.M. (Gardner 2008; Gardner 2019) – one may refer to Ashraf (M. Ashraf 2006) , Afshan (Afshan and Gardner 2013), Gardner (Gardner et al. 2006; Gardner and Theofanous 2008), Young (Young and Liu 2003; Young and Lui 2005), Real (Real and Mirambell 2005) or Theofanous (Theofanous and Gardner 2010). The C.S.M. certainly stands as an important improvement thanks to its strain-based approach, nicely mechanically suited to the non-linear material stress-strain response of this material.

Besides, another alternative design approach that shall as well be very satisfactory for stainless steel was recently developed: the Overall Interaction Concept (O.I.C.) (Boissonnade et al. 2017; Gérard et al. 2021; Hayeck et al. 2018; Li et al. 2022; Li and Boissonnade 2023). Initially intended at regular carbon steel, the O.I.C. proposes key features for our concerns here, namely proposing direct, continuous resistance predictions that may exceed the conventional plastic capacity. This paper summarizes efforts within the development of the O.I.C. for stainless steel I-shapes under simple or combined bending. As most of our reference results rely on advanced shell non-linear F.E. models, next Section 2 details how these models have been built and validated against experimental data, and then used along extensive numerical parametric studies. Section 3 further describes the proposed O.I.C.-based design rules and investigate their accuracy with respect to the numerical reference results. Eventually, Section 4 compares the performance of the present proposal and existing design rules, namely the European and American recommendations.

2. Development of Finite Element models

2.1 Shell F.E. models: basic features

Finite Element (F.E.) models were created in both (Abaqus 2011) and FINELg (FINELg 2011) software. Particular care was devoted for the models to be developed as similarly as possible, and they have been shown to provide equivalently accurate results (Gagné 2022). 4-nodes shell finite elements relying on Kirchhoff's theory in bending were used in FINELg while quadrilateral conventional shell elements with reduced integration S4R have been considered for ABAQUS. Linear Buckling Analyses (L.B.A., i.e., critical load calculations) were performed through a combined use of the subspace iteration method and of the Jacobi method; besides, Geometrically and Materially Non-linear with Imperfection Analyses (G.M.N.I.A., i.e., determination of ultimate capacities) were conducted by means of state-of-the-art numerical procedures involving typical Newton-Raphson iterations with out-of-balance residual corrections coupled with either the arc length method (for FINELg) or the Riks method (for ABAQUS), along with automatic loading strategies. Overall, the models were found suitable, accurate and efficient, namely with respect to achieving peak loads smoothly in G.M.N.I.A. (Gagné 2022).

Since only welded I-sections are of concern in the present paper, specific modelling features such as refinements in the web-flange area were not taken into account (Gérard et al. 2021), and the cross-sections were simply modelled through joining 3 plates together, cf. Figure 1 for example. Obviously, mesh sensitivity analyses were performed prior to resorting to series of F.E. computations, for both models and software. For FINELg computations, the inner capabilities of the shell quadrangular F.E. are known to be quite good and meshes such as in Figure 1a were shown sufficient; as per ABAQUS, meshes as in Figure 1b were found to provide the best

compromise between accuracy and a reasonable computation time – more details can be found in (Gagné 2022).

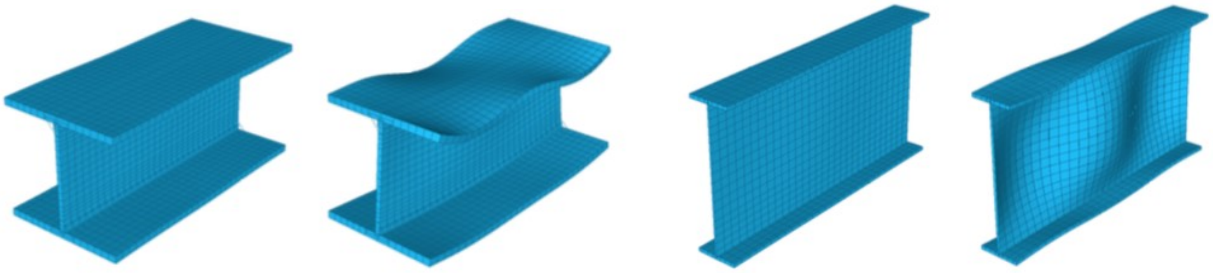

a)

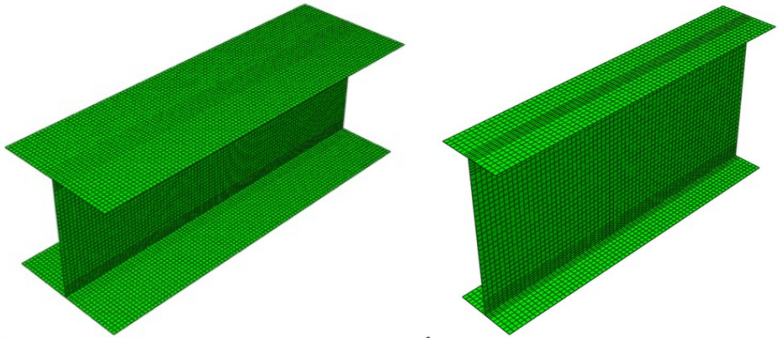

b)

Figure 1: Section modelling in – a) FINELg – b) ABAQUS

As for material behaviour, various material alloys were accounted for: austenitic 1.4301, ferritic 1.4003 and duplex 1.4362 stainless steel grades were considered in the analyses. Each material model was described by a so-called two-stage model (Gardner 2002) that follows the well-known Ramberg-Osgood expression up to the conventional proof-stress $\sigma_{0.2}$. However, a modified approach was adopted beyond $\sigma_{0.2}$ and up to the ultimate stress, as presented by Eq. (1) (Gardner and Nethercot 2004).

$$\begin{cases} \varepsilon = \dfrac{\sigma}{E_0} + 0.002 \cdot \left(\dfrac{\sigma}{\sigma_{0.2}} \right)^n & for \quad \sigma \le \sigma_{0.2} \\ \varepsilon = \dfrac{(\sigma - \sigma_{0.2})}{E_{0.2}} + \left(0.008 - \dfrac{\sigma_{1.0} - \sigma_{0.2}}{E_{0.2}} \right) \cdot \left(\dfrac{\sigma - \sigma_{0.2}}{\sigma_{1.0} - \sigma_{0.2}} \right)^{n'_{0.2,1.0}} & for \quad \sigma > \sigma_{0.2} \end{cases} \tag{1}$$

$$Where \quad E_{0.2} = \frac{\sigma_{0.2} \cdot E_0}{\sigma_{0.2} + 0.002 \cdot \ln E_0}$$

The different properties for each alloy are presented in Table 1, and Figure 2 shows the material responses of the 3 stainless steel grades considered herein.

Table 1: Material properties for the different stainless alloys considered.

Material grade	**1.4003**	**1.4301**	**1.4362**
E_0 [N/mm^2]	210 000	200 000	200 000
$E_{0.2}$ [N/mm^2]	16 458	16 092	33 333
$\sigma_{0.2}$ [N/mm^2]	250	210	400
$\sigma_{1.0}$ [N/mm^2]	286	252	458
n [–]	7	6	5
$n'_{0.2,1.0}$ [–]	3.3	2.7	3.35

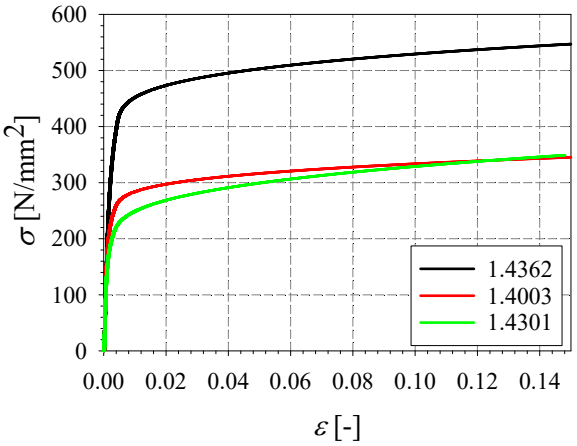

Figure 2: Material responses of the three stainless steel alloys considered.

In each finite element model, ideal fork support conditions were introduced. Such conditions allow both end sections to experience axial displacements (only one end), major-axis and minor-axis rotations as well as free warping. In addition, kinematic linear constraints relative to the axial degree of freedom were imposed to all nodes of the end sections but the 4 nodes at the flanges' tips, which remain axially free, allowing them to govern the deformation modes of the section (Gagné 2022; Gérard et al. 2021; Li and Boissonnade 2022). Accordingly, the Bernoulli assumption "plane sections remain plane" stays fulfilled, and no stress concentrations develop at the section ends. Figure 3 further illustrates these free/constrained relationships, and more details on these modelling features may be found in (Gagné 2022). In addition, transverse displacements of the web and flange nodes at the end sections were prevented, so as to avoid any local buckling in the direct vicinity of the end sections.

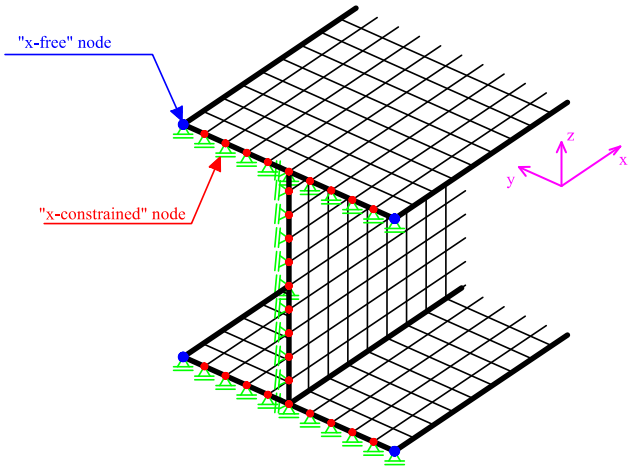

Figure 3: Modelling of end sections: transverse supports and linear constraints.

Geometrical imperfections were also considered in the F.E. models for G.M.N.I.A. calculations. They have been introduced through sinusoidal functions with 3 half-waves, as shown in Figure 4 – the selection of an appropriate shape for the initial geometrical imperfection may indeed be based on the 1st eigenmode (or a combination of several modes) or on sine distributions (Gérard et al. 2019; Gérard et al. 2021; Li and Boissonnade 2022; EN 1993-1-5, 2006); the latter was considered herein. The half-wavelength was set to the average between the amplitude of the web and the flange, i.e., respectively to $a_w = h - t_f$ and $a_f = b$ for welded sections, as recommended in (Gérard et al. 2019).

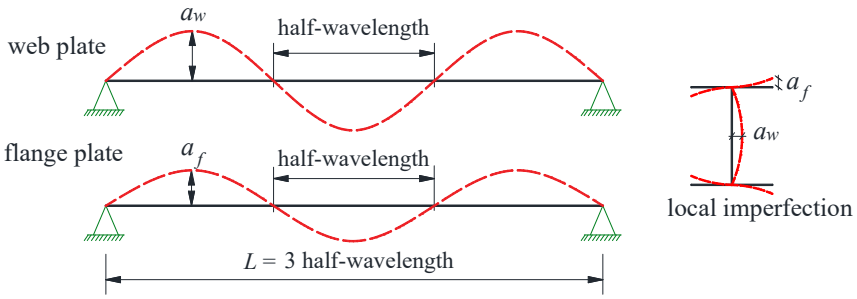

Figure 4: Sine-shaped functions for geometrical imperfections.

Besides, a numerical sub-study was carried out to characterize the associated imperfections' amplitudes to be considered in the model. For standard steel, various recommendations set the amplitude of the initial imperfection to be made dependent on the plate dimensions (EN 1993-1-5 2006; Johansson et al. 2007; Pavlovcic 2005) while others relate it to the plate thickness (Dawson and Walker 1972; Gardner et al. 2010; Schafer and Peköz 1998). Since both proposals make sense from a mechanical point of view, both types have been analysed. It was eventually decided (Gagné 2022) that an amplitude dependent on the plate dimension "*a*" shall be preferred over one dependent on the thickness "*t*", and this was adopted in the present study. In addition, as the data of the initial geometric imperfection as well as certain design codes (EN 1993-1-5 2006) recommend the use of a / 200, this amplitude was considered along parametric studies, cf. § 2.3.

Associated to the fabrication process considered here, a typical welded residual stresses pattern was introduced in the models, in all G.M.N.I.A. calculations (see Figure 5). Amplitudes and distribution shapes follow carbon steel recommendations (ECCS 1976), as observed by (Bredenkamp et al. 1992); albeit relatively usual, this pattern bears the particularity that self-equilibrium is ensured on a plate-per-plate basis, through adequate values of γ_1 and γ_2 that depend on the section's dimensions.

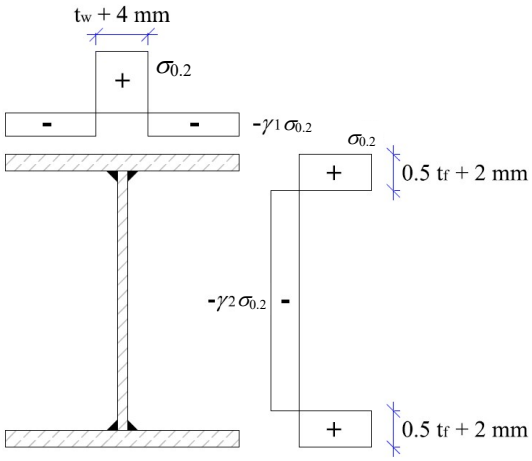

Figure 5: Residual stresses pattern considered (welded).

2.2 Validation vs test data

In order to ensure the pertinence of the numerical models while avoiding experimental testing which would require significant resources, model validation was carried out on the basis of available experimental test data. The first series of tests referred to here was carried out on austenitic and duplex stainless steels in compression only (Yuan et al. 2014); the second set of tests focuses on lean duplex stainless steel sections under pure compressive forces or in 4-point major-axis bending (Saliba and Gardner 2013). Finally, the third series of experimental tests focuses on high-chromium steels under compression, major-axis bending and minor-axis bending (Sun and Zhao 2019). Accordingly, various sources, materials, research teams and load cases were considered, which provides a better legitimacy to the validation results detailed in the following.

Different specific assumptions were considered in order to replicate the testing conditions as accurately as possible. First, the measured dimensions and lengths used were introduced in the models, as detailed in Table 2. Further, initial geometrical imperfections were introduced through sine functions (as described in section 2.1), and both *measured* web and flanges amplitudes were considered, as well as a period of sinusoidal shape associated with the imperfections as presented in section 2.5. Residual stresses pattern as shown in Figure 5 were also considered. Additionally, measured material properties were taken into account, through Eq. (1) format and Table 4 (measured) coefficients.

Particular attention was also paid to the support conditions: in order to account for the presence of typical end plates, end sections' warping and rotations about both principal axes were fixed. Regarding 4-point bending arrangements, transverse stiffeners were welded on the specimen yet not included in the numerical model, so that only the segment in between two stiffeners was modeled (Gagné 2022).

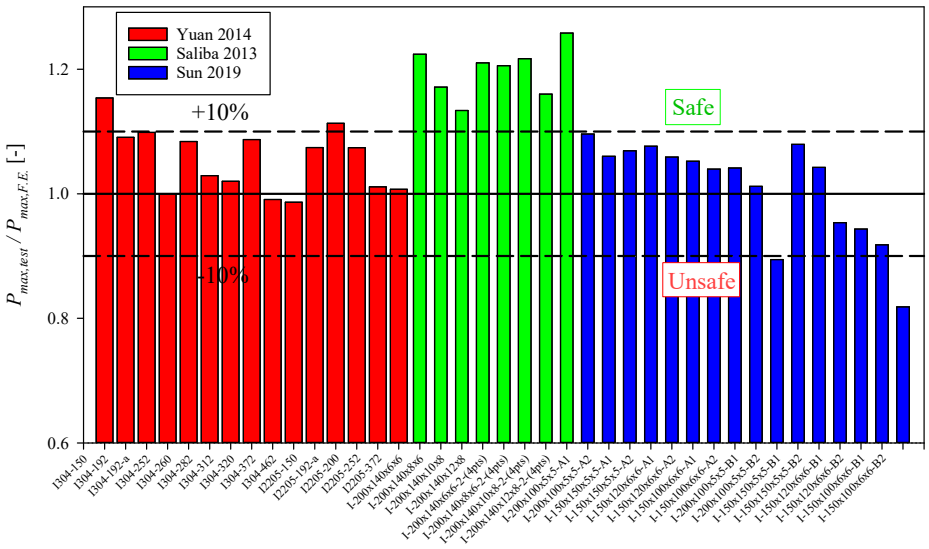

Figure 6: Summary of test vs F.E. results.

The results of the comparison are summarized in Figure 6. They reveal quite good resistance prediction levels for the F.E. models, as an average of 6.6% difference between test and F.E. results is reported, on the safe side, when all sources of test data are combined. Figure 6 also reveals that many results lie within a 10% margin, except for the tests conducted by (Saliba and Gardner 2013), where the presence of transverse stiffeners is thought to be the main source of the discrepancies.

Finally, Figure 7 provides several load-displacement examples that have been "translated" into stress-strain figures so as to propose several tests on a single plot and Figure 8 compares the load-end shortening curves of stub column specimens. Here again good correspondence between the numerical sources and the reference test data is observed, in terms of peak load, initial stiffness, post peak behaviour, etc. Accordingly, the F.E. models are deemed fit for being substituted to physical testing and have been thoroughly used within numerical parametric studies, as detailed in the next paragraphs.

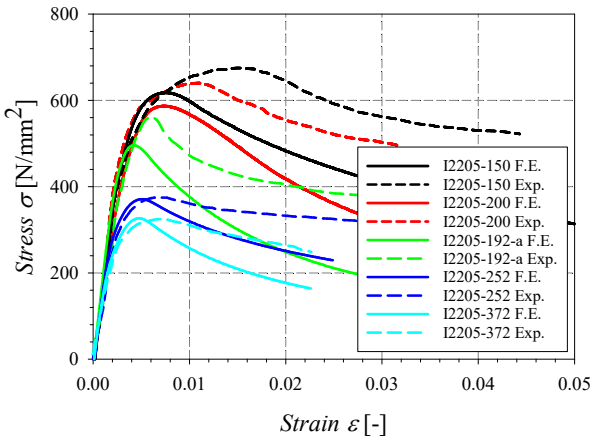

Figure 7: Comparison between numerical and experimental stress-strain responses for specimens made of steel grade 1.4462 (Yuan et al., 2014).

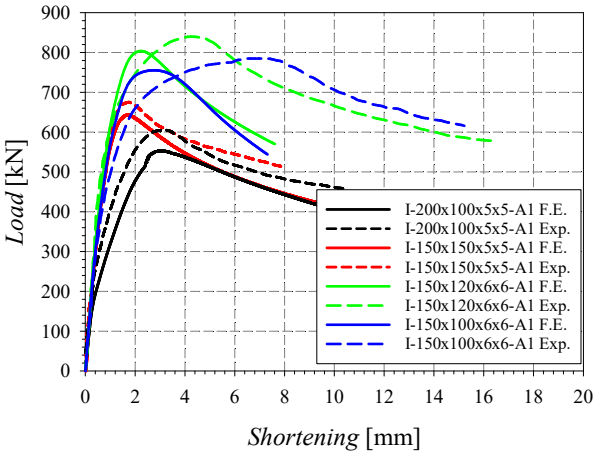

Figure 8: Load-end shortening curves of stub column specimens − First series of specimen "A1" (Sun and Zhao, 2019).

Table 2: Measured dimensions of tested specimens.

Ref.	Specimen	Load case	b_t [mm]	b_b [mm]	h [mm]	$t_{f,t}$ [mm]	$t_{f,b}$ [mm]	t_w [mm]	r [mm]	L [mm]
(Yuan et al., 2014)	I304-150	N	149.5	149.5	149.5	10	10	6	5	449.6
	I304-192	N	185.2	185.3	193.8	6	6	6	5	598
	I304-192-a	N	126.4	126.1	194.2	6	6	6	5	601.1
	I304-252	N	246.1	245.3	253.2	6	6	6	5	779.9
	I304-260	N	165.4	166	258.9	10	10	6	5	779.9
	I304-282	N	185.7	185.5	282.9	6	6	6	5	850.4
	I304-312	N	305.5	305.5	313.7	6	6	6	5	951.6
	I304-320	N	205.7	205.5	319.6	10	10	6	5	961.6
	I304-372	N	246.1	246	373.3	6	6	6	5	1117.8
	I304-462	N	185.8	186.2	462.5	6	6	6	5	1400.7
	I2205-150	N	149	151	150.6	10.2	10.2	6	5	449.4
	I2205-192-a	N	126.2	125.4	193.1	6	6	6	5	600
	I2205-200	N	124.8	125	200.5	10.2	10.2	6	5	601.4
	I2205-252	N	245	245.5	252.8	6	6	6	5	780
	I2205-372	N	245	245	372.8	6	6	6	5	1117
(Saliba and Gardner, 2013)	I-200x140x6x6	N	138.9	138.9	202.0	6.1	6.1	6.0	5	600.4
	I-200x140x8x6	N	139	139	201.0	8.0	8.0	6.0	5	600.4
	I-200x140x10x8	N	139	139	199.1	10.3	10.3	8.0	6	600.3
	I-200x140x12x8	N	139.3	139.3	199.1	12.6	12.6	8.1	6	600.2
	I-200x140x6x6-2	M_y	138.6	138.6	202.0	6.1	6.1	6.0	5	1000
	I-200x140x8x6-2	M_y	139.3	139.3	200.6	8.1	8.1	6.0	5	1000
	I-200x140x10x8-2	M_y	139	139	199.2	10.2	10.2	8.0	6	1000
	I-200x140x12x8-2	M_y	139.6	139.6	198.8	12.3	12.3	8.1	6	1000
(Sun and Zhao, 2019)	I-200x100x5x5-A1	N	99.2	99.2	199.7	5	5	5.0	2	600.2
	I-200x100x5x5-A2	N	99.2	99.2	199.6	5.0	5.0	5.0	2	600.5
	I-150x150x5x5-A1	N	149.0	149.0	149.5	5.0	5.0	5.1	2	448
	I-150x150x5x5-A2	N	149.1	149.1	149.6	5.1	5.0	5.1	2	447.5
	I-150x120x6x6-A1	N	119.3	119.3	149.2	6.0	6.0	6.0	2	450
	I-150x120x6x6-A2	N	119.3	119.3	149.4	6.0	6.0	6	2	448.4
	I-150x100x6x6-A1	N	99.4	99.4	149.3	6.1	6.1	6.2	2	448.3
	I-150x100x6x6-A2	N	99.4	99.4	149.3	6.1	6.1	6.1	2	448.1
	I-200x100x5x5-B1	M_y	99.3	99.3	199.4	4.9	4.9	5.1	2	600
	I-200x100x5x5-B2	M_z	99.0	99.0	199.2	5.1	5.1	4.9	2	600
	I-150x150x5x5-B1	M_y	149.0	149.0	149.9	5.1	5.1	5.1	2	600
	I-150x150x5x5-B2	M_z	148.8	148.8	150.3	5.1	5.1	5.2	2	600
	I-150x120x6x6-B1	M_y	119.2	119.2	149.4	6.0	5.9	5.9	2	600
	I-150x120x6x6-B2	M_z	119.5	119.5	148.9	6.0	6.0	6.1	2	600
	I-150x100x6x6-B1	M_y	99.2	99.2	149.6	6.1	6.1	6.1	2	600
	I-150x100x6x6-B2	M_z	99.5	99.5	149.2	6.1	6.1	6.1	2	600

Table 3: Measured initial geometrical imperfections and test / F.E. peak loads.

Ref.	Specimen	In top flange [mm]	In bottom flange [mm]	In web [mm]	Nb of half-periods [–]	Period [mm]	Test / F.E. [–]
(Yuan et al., 2014)	I304-150	0.55	0.55	0.19	3	149.8	1.15
	I304-192	1.05	0.95	0.39	3	199.3	1.09
	I304-192-a	0.53	0.79	0.28	3	200.3	1.10
	I304-252	1.17	0.82	0.24	3	259.9	1.00
	I304-260	0.38	0.67	0.49	3	259.9	1.08
	I304-282	-0.84	-0.87	0.35	3	283.4	1.03
	I304-312	1.51	0.56	-0.32	3	317.2	1.02
	I304-320	-0.71	-0.65	0.46	3	320.5	1.09
	I304-372	1.2	0.76	0.32	3	372.6	0.99
	I304-462	0.59	0.9	1.11	4	350.2	0.99
	I2205-150	0.59	0.56	0.21	3	149.8	1.07
	I2205-192-a	0.31	0.6	0.26	3	200.0	1.11
	I2205-200	0.27	0.71	0.22	3	200.5	1.07
	I2205-252	0.55	0.31	0.22	3	260.0	1.01
	I2205-372	0.77	0.52	0.52	3	372.3	1.01
(Saliba and Gardner, 2013)	I-200x140x6x6	0.301	0.2885	0.2025	3	200.1	1.22
	I-200x140x8x6	0.1735	0.12	0.3425	3	200.1	1.17
	I-200x140x10x8	0.137	0.2325	0.4075	3	200.1	1.13
	I-200x140x12x8	0.202	0.237	0.2065	3	200.1	1.21
	I-200x140x6x6-2	0.495	0.426	0.241	5	200.0	1.21
	I-200x140x8x6-2	0.125	0.12	0.284	6	166.7	1.22
	I-200x140x10x8-2	0.125	0.27	0.489	6	166.7	1.16
	I-200x140x12x8-2	0.132	0.174	0.154	6	166.7	1.26
(Sun and Zhao, 2019)	I-200x100x5x5-A1	0.33	0.33	0.17	4	150.1	1.10
	I-200x100x5x5-A2	0.52	0.52	0.14	4	150.1	1.06
	I-150x150x5x5-A1	0.23	0.23	0.13	3	149.3	1.07
	I-150x150x5x5-A2	0.16	0.16	0.06	3	149.2	1.08
	I-150x120x6x6-A1	0.1	0.1	0.09	3	150.0	1.06
	I-150x120x6x6-A2	0.12	0.12	0.07	3	149.5	1.05
	I-150x100x6x6-A1	0.15	0.15	0.04	3	149.4	1.04
	I-150x100x6x6-A2	0.14	0.14	0.06	3	149.4	1.04
	I-200x100x5x5-B1	0.28	0.28	0.15	4	150.0	1.01
	I-200x100x5x5-B2	0.21	0.21	0.15	4	150.0	0.89
	I-150x150x5x5-B1	0.42	0.42	0.11	4	150.0	1.08
	I-150x150x5x5-B2	0.5	0.5	0.17	4	150.0	1.04
	I-150x120x6x6-B1	0.33	0.33	0.22	4	150.0	0.95
	I-150x120x6x6-B2	0.44	0.44	0.09	4	150.0	0.94
	I-150x100x6x6-B1	0.36	0.36	0.13	4	150.0	0.92
	I-150x100x6x6-B2	0.34	0.34	0.11	4	150.0	0.82

Table 4: Measured material properties from the different test series considered.

Ref.	Grade	t [mm]	E_0 [N/mm²]	$\sigma_{0.2}$ [N/mm²]	$\sigma_{1.0}$ [N/mm²]	σ_u [N/mm²]	n [–]	$n'_{0.2,1.0}$ [–]
(Yuan et al., 2014)	1.4301	6.00	188 600	312.6	354.4	695.7	5.8	2.7
		10.00	188 800	328.5	379.4	659.8	6.9	2.7
	1.4462	6.00	193 200	605.6	665.0	797.9	7.4	2.8
		10.20	191 200	574.8	651.2	775.0	6.7	2.8
(Saliba and Gardner, 2013)	1.4162	6.01	193 500	516.0	557.5	727.5	10.7	2.2
		8.08	203 000	504.0	545.5	727.5	12.2	2.2
		10.09	216 500	501.0	557.0	768.5	11.8	2.2
		12.4	205 500	456.5	506.0	722.5	10.5	2.4
(Sun and Zhao, 2019)	1.4420	5.00	187 800	326.0	379.0	688.0	3.2	2.9
		6.00	187 900	339.0	398.0	718.0	3.5	2.5

2.3 Parametric studies

The numerical models being validated, a great number of both L.B.A. and G.M.N.I.A. numerical simulations have been performed, so as to gather information on (i) the critical buckling response of WF stainless steel sections and on (ii) their ultimate (failure) loads, respectively.

Grades 1.4301, 1.4003 and 1.4362, respectively corresponding to austenitic, ferritic and duplex stainless steel alloys, were considered. A total of 88 different cross-section geometries was considered, for a wide range of shapes, dimensions and section slenderness to be covered. 30 of them are available in current European catalogues: 10 IPE, 10 HEA and 10 HEM were used in the study. Besides, additional sections were obtained through modifying the later ones to create a wider range of slenderness. 10 IPES and 10 HEAS were invented through a 30% reduction in the thickness of the dominant element in the section (webs for IPE shapes and flanges for HEA shapes). Also, 30 additional cross-sections (SS) have been created, where both flanges and web thickness were 30% reduced. These sections were intended to get results for cases where local buckling and the associated initial imperfections are more influential while keeping other dimensions constant, in particular the h / b ratios. All selected sections aim at being beam or column shapes, or intermediaries between the two.

Both simple and combined load cases have been considered, and two different parameters were used to characterize the load combination (see Eq. (2)). The first parameter, referred to as n, represents the relative level of axial compression; the second parameter, α_{biax}, corresponds to the degree of biaxial bending which can be defined through "m_y" and "m_z", the relative amounts of major and minor-axis bending, respectively. For biaxial bending cases, α_{biax} allows to represent the respective relative importance of each type of bending, either about the major or about the minor axis: a value of 0° indicates major-axis bending only, while a value of 90° refers to pure minor-axis bending. Some 4 values for n and 5 for α_{biax} have been chosen, as reported in Table 5; it is to be noted that special attention was paid for compression + biaxial cases to evenly span the entire set of possible situations (Gagné 2022). Overall, a total of 3 833 non-linear shell F.E.

calculations have been performed and shall serve as a reference to assess the merits of the proposed O.I.C.-based design approach.

$$\begin{cases} n = \dfrac{N_{ini}}{N_{pl}} \\ \tan\left(\alpha_{biax}\right) = \dfrac{M_{z,ini}/M_{z,pl}}{M_{y,ini}/M_{y,pl}} = \dfrac{m_z}{m_y} \end{cases} \tag{2}$$

Table 5: Parameters considered to vary load cases.

n	0; 0.30; 0.80; 1
α_{biax}	0; 30; 50; 70; 90

3. O.I.C.-based design approach for combined load cases

3.1 Bases of the O.I.C. approach and proposal for combined load cases

The collected F.E. results are meant to serve as a reference for the assessment of a new design approach, based on the Overall Interaction Concept (O.I.C.). This approach relies on the 5 steps illustrated in Figure 9; as a particular point, it shall be emphasized that Step 3 defines a new local slenderness parameter λ_L (sometimes denoted as "local relative slenderness") that aims at taking the balance between plastic resistance (which is the maximum resistance the section may provide when buckling and imperfections are ignored) and the section's local buckling load (which constitutes a 2nd limit case where yielding and imperfections are not taken into account). Also, the use of load ratios R_{pl}, $R_{cr,L}$ and $R_{b,L}$ allows the approach to remain general enough whatever the load case. For example, R_{pl} defines as the load ratio by which the initial loading shall be multiplied the reach the section's plastic capacity. Accordingly, the final design check consists in the ultimate load ratio $R_{b,L}$ examined to be higher than unity, indicating that the actual loading shall be increased to reach the real, ultimate capacity ($R_{b,L}$ accounts for yielding, local buckling and imperfections). When $R_{b,L} < 1.0$, the loading acting on the section is too high and shall be reduced to ensure safety.

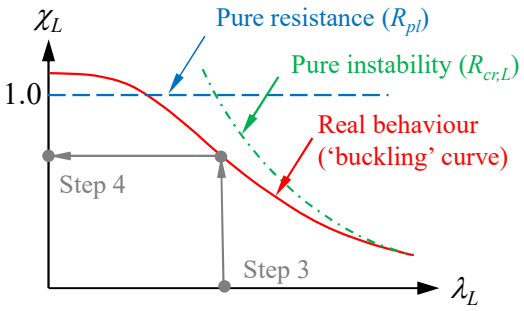

Step 1: R_{pl} Load ratio to reach the plastic 'resistance' limit

Step 2: $R_{cr,L}$ Load ratio to reach the critical 'instability' limit

Step 3: $\lambda_L = \sqrt{R_{pl} / R_{cr,L}}$

Step 4: $\chi_L = f°(\lambda_L)$

Step 5: $R_{b,L} = \chi_L \cdot R_{pl}$

Figure 9: Principles of the O.I.C. and application steps (case of *local* buckling here).

These O.I.C. design steps can also conveniently be summarized as in Figure 10's flow chart, for design purposes. More details and background explanations on the O.I.C. may be found in (Ayrton and Perry 1886; Boissonnade et al. 2017; Li and Boissonnade 2022; Li and Boissonnade

2023). Of practical interest, one may note that (i) both $R_{cr,L}$ and R_{pl} factor may be obtained through advanced tools (e.g., F.E. software) or through classical formulae, and that (ii) use of cross-section classification and of the Effective Width Method is no more necessary. In addition, the approach may be seen to provide direct and smooth resistance predictions, from plastic to slender cross-section shapes.

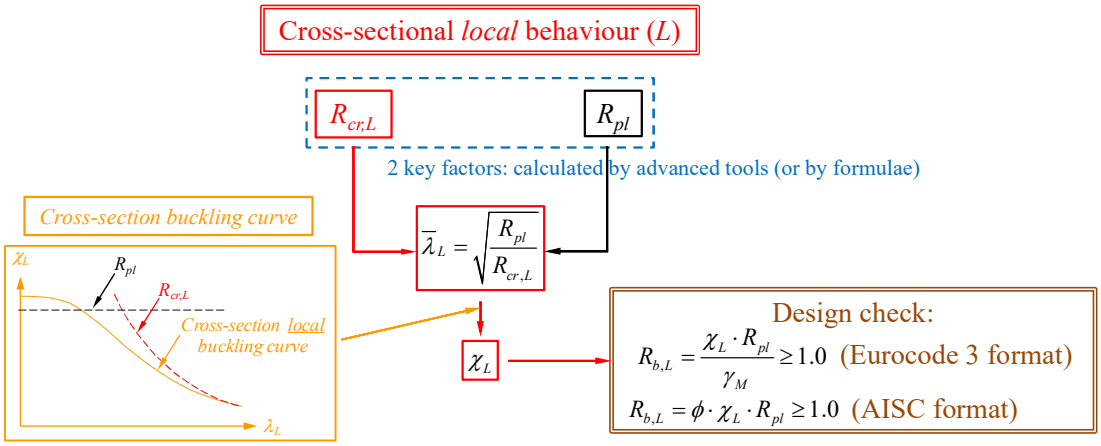

Figure 10: O.I.C. design flow chart for cross section resistance.

A key aspect in this approach is the definition of suitable local buckling curves, as there shall exist more than one: it would indeed show rather uneconomical to rely on a unique, safe-sided one. Experimental and numerical results indeed show a relative scatter of results (Gagné et al. 2020) to be addressed. Accordingly, preliminary studies have been carried out to identify leading parameters responsible for the scatter, and these were found to be dependent on section's geometrical characteristics rather than on material properties (in particular, the influence of the material grade was found sufficiently accounted for in the O.I.C. approach, namely through factor R_{pl}) – see Eq. (3).

$$\gamma = 0.001 \cdot \left(\frac{h}{t_w}\right) \cdot \left(\frac{b}{t_f}\right) \cdot \left(\frac{t_w}{t_f}\right) \tag{3}$$

In the present context, two different design approaches for stainless steel I-shapes have been developed: (i) a 2-step one that is governed by strain at low λ_Ls while λ_L-driven for high slenderness as well as (ii) an all λ_L-driven applicable to the whole λ_L range. Whereas the 2nd one is "classical" – used for decades for flexural or lateral torsional buckling for example –, the 1st approach consists in a 2-step procedure to the determination of χ_L: Step 1 relates the section's relative slenderness λ_L calculated as in Figure 10 to the strain ratio $\varepsilon_{peak} / \varepsilon_y$, where ε_{peak} is the strain level at peak load and ε_y is the strain at $\sigma_{0.2}$. This follows the main idea of the Continuous Strength Method (Gardner 2008) and is mechanically sound for plastic/compact sections, and therefore applies for $\lambda_L < \lambda_0$ where λ_0 is a reference slenderness limit. In a 2nd step, the strain ratio connects with χ_L to get the ultimate resistance $R_{b,L} = \chi_L \cdot R_{pl}$. The set of equations in Eq. (4) provides an example of final design expression that was obtained following this approach for sections under simple compression, as a function of the steel grade.

$$\begin{cases} \chi_L = 1.49 - 1.105 \cdot \lambda_L & for\ grade\ 1.4301 \\ \chi_L = 1.307 - 0.68 \cdot \lambda_L & for\ grade\ 1.4003 \\ \chi_L = 1.368 - 0.806 \cdot \lambda_L & for\ grade\ 1.4362 \end{cases} \quad (4)$$

Figure 11 further illustrates the 2-step procedure used for obtaining Eq. (4) expressions. Identical procedures were followed to reach design expressions for all simple load cases, which are summarized in Table 6.

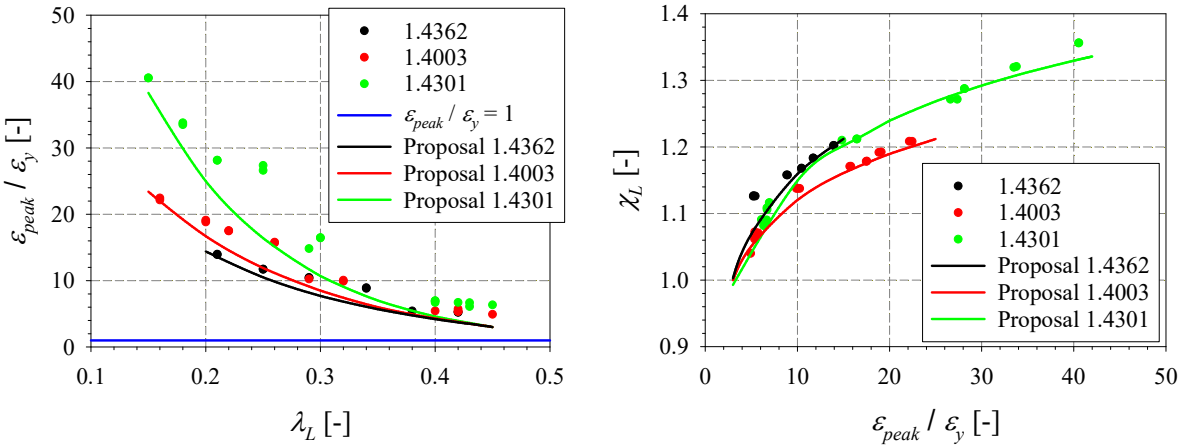

Figure 11: Principle of two-step procedure for $\lambda_L \leq \lambda_0$ (compression cases).

Table 6: Summary of design expression for simple load cases.

Load case	Compression N	Major-axis bending M_y	Minor-axis bending M_z
Reference slenderness λ_0	$\lambda_0 = 0.45$	$\lambda_0 = 0.50$	$\lambda_0 = 0.55$
For compact sections $\lambda_L \leq \lambda_0$	$\begin{cases} \chi_L = 1.49 - 1.105 \cdot \lambda_L & for\ 1.4301 \\ \chi_L = 1.307 - 0.68 \cdot \lambda_L & for\ 1.4003 \\ \chi_L = 1.368 - 0.806 \cdot \lambda_L & for\ 1.4362 \end{cases}$	$\begin{cases} \chi_L = 1.92 - 4.20 \cdot \lambda_L + 4.97 \cdot \lambda_L^2 & for\ 1.4301 \\ \chi_L = 1.68 - 3.08 \cdot \lambda_L + 3.64 \cdot \lambda_L^2 & for\ 1.4003 \\ \chi_L = 1.81 - 3.64 \cdot \lambda_L + 4.30 \cdot \lambda_L^2 & for\ 1.4362 \end{cases}$	$\begin{cases} \chi_L = 2.41 - 6.15 \cdot \lambda_L + 7.28 \cdot \lambda_L^2 & for\ 1.4301 \\ \chi_L = 3.76 - 10.07 \cdot \lambda_L + 11.92 \cdot \lambda_L^2 & for\ 1.4003 \\ \chi_L = 3.76 - 10.07 \cdot \lambda_L + 11.92 \cdot \lambda_L^2 & for\ 1.4362 \end{cases}$
For non-compact sections $\lambda_L \geq \lambda_0$	$\phi_L = 0.5 \cdot \left[1 + \alpha_L \cdot (\lambda_L - \lambda_0) + \lambda_L^{\delta}\right]$	$\chi_L = \dfrac{1}{\phi_L + \sqrt{\phi_L^2 - \lambda_L^{\delta}}}$	$\gamma = 0.001 \cdot \left(\dfrac{h}{t_w}\right) \cdot \left(\dfrac{b}{t_f}\right) \cdot \left(\dfrac{t_w}{t_f}\right)$
	$\alpha_L = 0.15 \cdot \gamma + 0.07$ $\delta = 0.1 \cdot \gamma + 0.05$	$\alpha_L = 0.15 \cdot \gamma + 0.02$ $\delta = 0.07 \cdot \gamma$	$\alpha_L = 0.25$ $\delta = 0.35$

In terms of performance and accuracy, Figure 12 provides examples of results for compression and major-axis bending cases, for plastic/compact shapes – $\lambda_L \leq \lambda_0$. As can be seen, all proposals lead to safe yet accurate χ_L values, which are found quite close to the reference F.E. ones (dots). More details can be found in (Gagné et al. 2020; Gagné 2022).

For the most slender sections, characterized by $\lambda_L \geq \lambda_0$, a $\lambda_L - \chi_L$ relationship is established through a modified Ayrton-Perry approach (Boissonnade et al. 2017; Gagné et al. 2020). This

rather well-established format is recalled in the last row of Table 6, where factor δ aims at specifically accounting for plate post-buckling effects, the latter being also observed in the resistance of WF sections – cf. Section 4. Parameter α_L stands as a general (cross-sectional) imperfection factor, and, together with δ, is made a function of geometrical parameter γ. Examples of results for $\lambda_L \geq \lambda_0$ cases are given in Figure 13a for compression and in Figure 13b for major-axis bending. As can be seen, the accuracy is pretty good when compared to the numerical results – please note that in Figure 13, all "Proposal" curves are relative to lower bounds of δ, i.e., they constitute safe limits of the individual data points. Deeper analyses and results may be found in (Gagné et al. 2020).

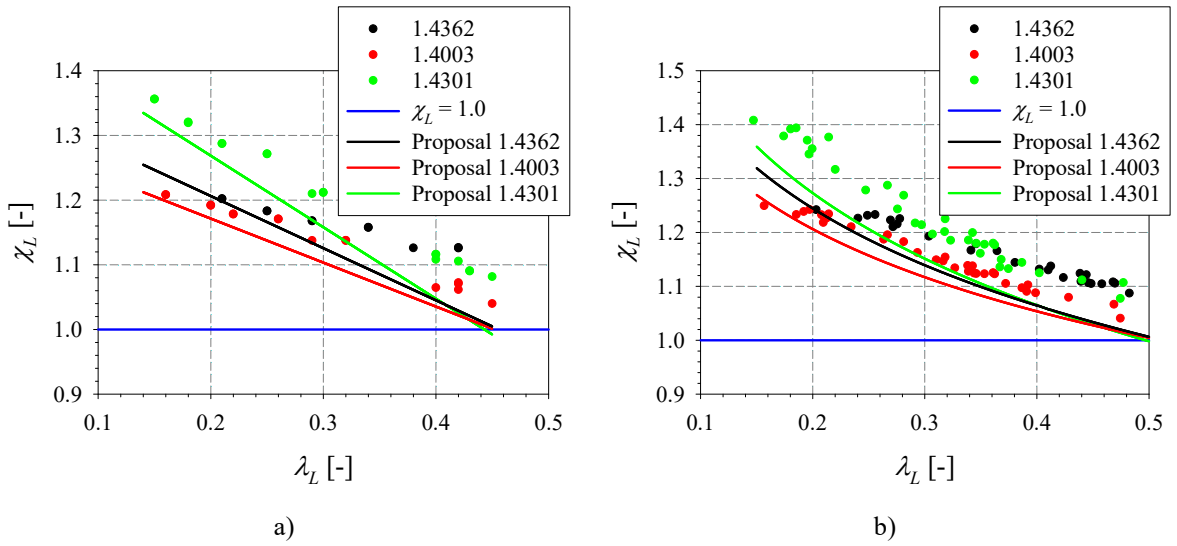

Figure 12: Performance of proposed approach for $\lambda_L \leq \lambda_0$ – a) Compression – b) Major-axis bending.

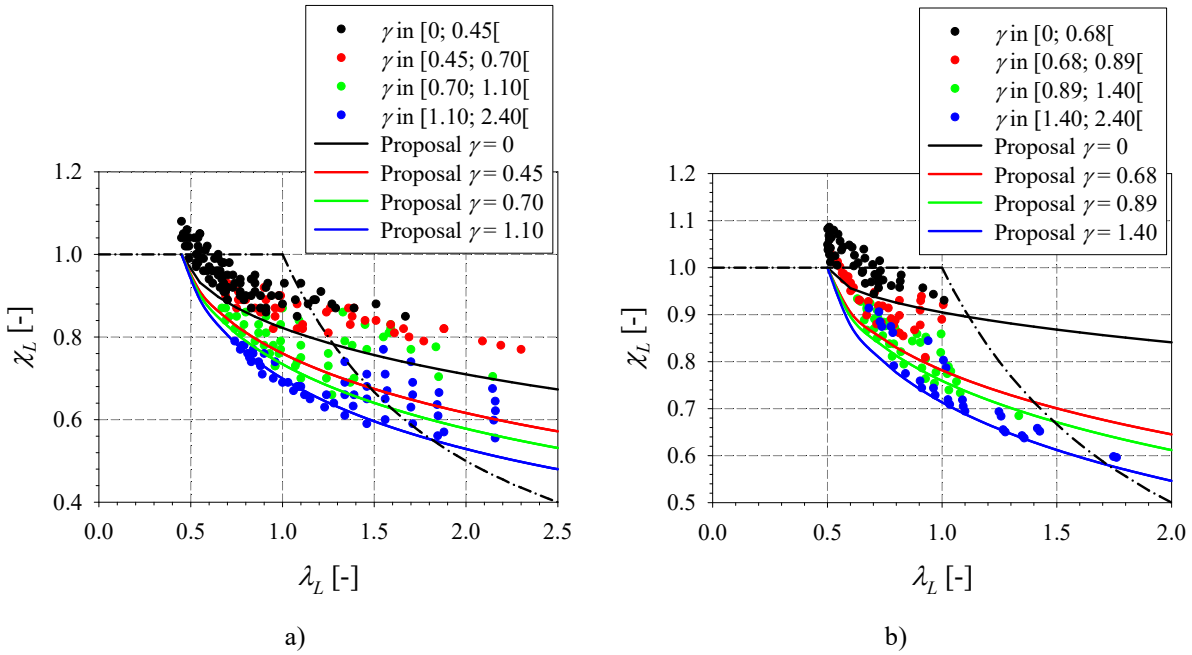

Figure 13: Performance of proposed approach for $\lambda_L \geq \lambda_0$ – a) Compression – b) Major-axis bending.

3.2 Extension to combined load cases

The format of the proposed O.I.C.-based design approach can be extended to combined loading situations on the basis of Figure 14 system of spherical coordinates and 3D resistance surface. Each axis refers to a relative amount of an internal force (either relative axial compression n or relative major or minor-axis bending moments m_y and m_z, cf. Eq. (2)), and a resistance surface is defined on this 3D loading space so that any load combination leading to a point below this surface indicates that the design under these forces is safe-sided, while a point lying on this surface means that maximum resistance is just reached – obviously, loading points outside/above this surface denotes that capacity is exceeded and that loading shall be reduced.

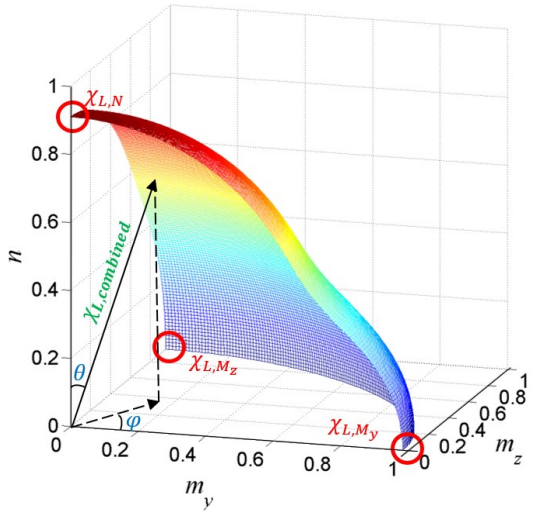

Figure 14: 3D resistance surface.

With the use of spherical coordinates, Eq. (5) allows to nicely characterize the shape of this surface. So-called "end points" are relative to simple load cases and are characterized by $\chi_{L,N}$, $\chi_{L,My}$ and $\chi_{L,Mz}$ reduction factors. In addition, q factors in Eq. (5) authorize adjustments in the surface's shape: indeed, material yielding tends to give a convex shape to the surface, while local buckling effects leads to a more concave form. Accordingly, q factors address either the overall surface shape (q_1) or local modifications of the geometry which are load-dependant (q_2 to q_6).

$$\chi_{L,combined} = \left[\left(\chi_{L,N} \cdot \cos(\theta)^{q_2} \right)^{q_1} + \left(\chi_{L,My} \cdot \sin(\theta)^{q_3} \cdot \cos(\phi)^{q_4} \right)^{q_1} + \left(\chi_{(L,Mz)} \cdot \sin(\theta)^{q_5} \cdot \sin(\phi)^{q_6} \right)^{q_1} \right]^{\frac{1}{q_1}} \quad (5)$$

Each of the q coefficient has been numerically adjusted to fit the reference F.E. data, while keeping expressions simple. Eventually, the coefficients presented in Table 7 summarize the proposed factors.

Table 7: q factors for combined loading situations.

q_1 [–]	q_2 [–]	q_3 [–]	q_4 [–]	q_5 [–]	q_6 [–]
4	1	2	0	6	5

The results for the 3 120 cases of combined loading cases considered here are shown in Figure 15a, which summarizes the frequencies of the $\chi_{L,F.E.}$ / $\chi_{L,O.I.C.}$ ratio along various accuracy intervals. A ratio above 1.0 indicates a safe resistance prediction, whereas ratios < 1.0 relate to

unsafe cases. Figure 15a shows that the proposed O.I.C. design approach provides excellent resistance predictions, both accurate and safe-sided with a narrow standard deviation. Also, Figure 15b further details the behaviour of the proposed approach in splitting the results by load cases; it shows the consistent trend of the O.I.C. approach to provide both (i) low amounts of unsafe predictions (values worse than 3% on the unsafe side) and (ii) a limited number of cases with over-predictions (values of the $\chi_{L,F.E.} / \chi_{L,O.I.C.}$ ratio > 1.10), regardless of the load case considered. Next Section 4 further compares these results with existing design approaches.

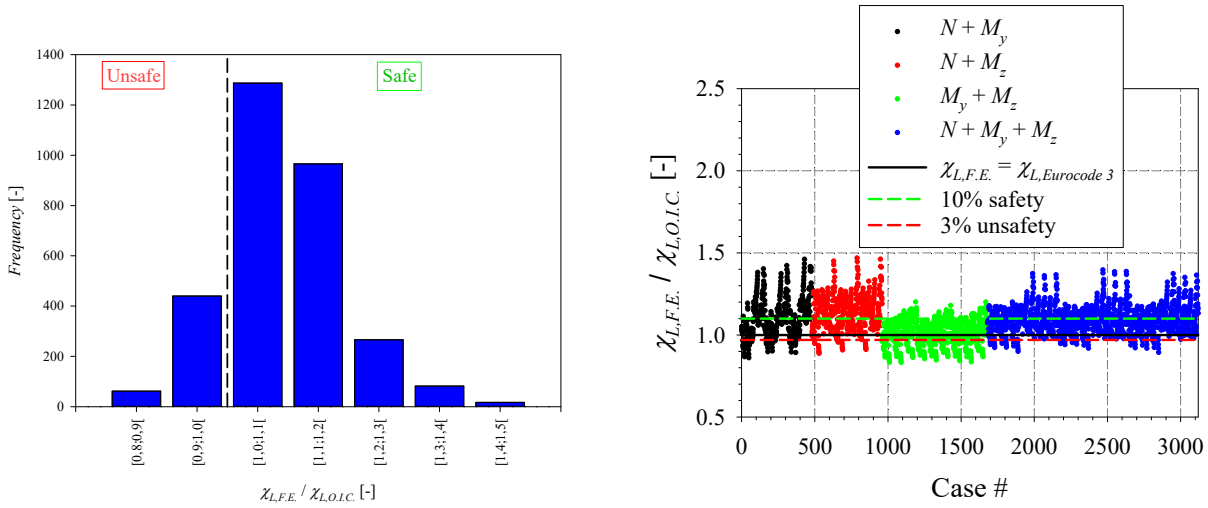

a) b)

Figure 15: a) Accuracy of proposal for combined load cases (all cases included) b) Performance of proposal based on load cases.

4. Performance of proposed approach compared to existing design approaches

The overall performance of the proposed design proposal can be summarized through Figure 16, Figure 17 and Table 8. First, simple compression load cases are considered, and the relative results are proposed in Figure 16a: while it can be observed that all 3 design proposals (O.I.C. approach, Eurocode 3 and A.I.S.C.) behave relatively well in terms of accuracy and consistency, the O.I.C.-based approach is seen to provide much less unsafe resistance predictions. Figure 16b, relative to bending about the major-axis M_y, shows more scattered resistance estimates for Eurocode 3 and A.I.S.C., both on the unsafe and on the over-safe side In contrast, O.I.C. calculations provide accurate and economical resistance predictions, with a high level of consistency.

As per combined loading situations, detailed statistical results are gathered in Table 8, and Figure 17a to Figure 17c provide summary/load case dependent results. Overall, they show that the O.I.C.-based approach significantly improves design predictions: for any type of load combination, the O.I.C. results are seen more accurate, more consistent, less unsafe and more economical than their European and American counterparts. Eurocode 3 indeed is seen to provide more scattered and generally over-safe resistance estimates, whatever the load case. In particular, Table 8 shows very high values of the mean $\chi_{L,F.E.} / \chi_{L,Eurocode\ 3}$ ratio as well as significant percentages of results above 20% conservatism for Eurocode 3. Oppositely, A.I.S.C. rules are seen to lead to quite important amounts of unsafe predictions, whatever the load case – Figure 17c also shows that combinations where bending is predominant lead to the most unsafe

results. For $N + M_y + M_z$ case, A.I.S.C. is even seen to provide close to 70% of its predictions with beyond 3% unsafe resistance estimates. In terms of consistency, the O.I.C.-based proposal is seen to give the lowest Coefficients of Variation (C.O.V.) for every combined load case considered, which further confirms the better performance of the latter approach.

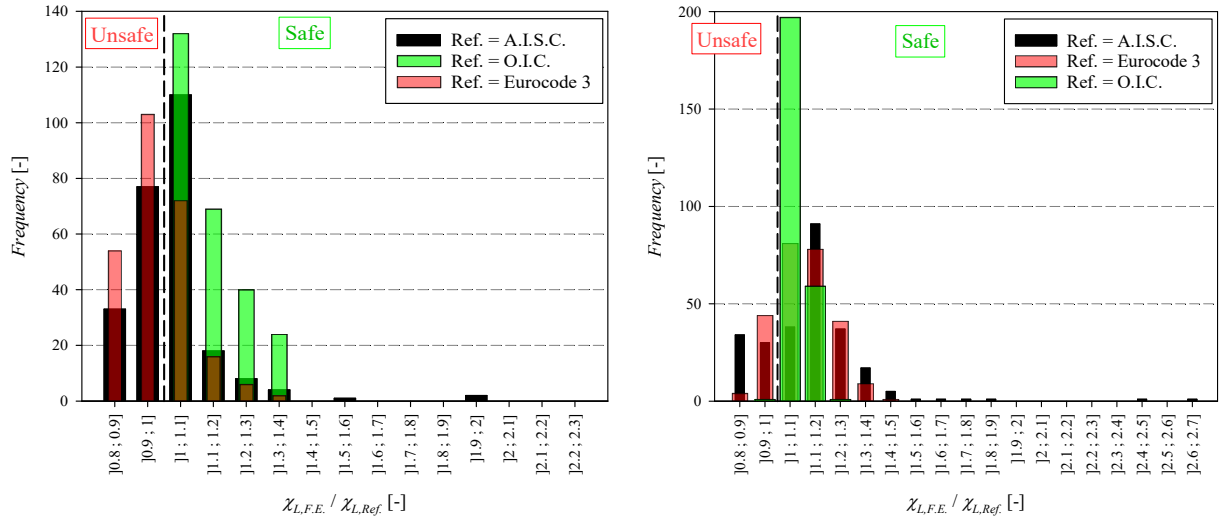

a) b)

Figure 16: Performance of proposed approach vs existing ones (Eurocode 3 and A.I.S.C.) for simple load cases – a) Compression N – b) Major-axis bending M_y.

Table 8: Statistical results for the performance of the various design approaches.

Load case	Proposal	Mean [–]	C.O.V. [%]	Nb tot. [–]	Max. [–]	Min. [–]	% < 0.97 [%]	% > 1.10 [%]	% > 1.20 [%]
$N + M_y$	O.I.C.	1.10	10.7%	480	1.46	0.86	11.0%	46.5%	19.0%
	Eurocode 3	1.08	12.2%	480	1.53	0.85	21.7%	38.1%	19.8%
	A.I.S.C.	1.07	16.9%	480	1.85	0.75	28.3%	38.8%	18.3%
$N + M_z$	O.I.C.	1.14	9.0%	480	1.47	0.89	4.0%	64.2%	30.2%
	Eurocode 3	1.42	16.5%	480	1.96	0.99	0.0%	95.6%	79.4%
	A.I.S.C.	1.03	18.4%	480	1.96	0.75	39.2%	20.0%	12.7%
$M_y + M_z$	O.I.C.	1.03	7.3%	720	1.20	0.83	23.2%	16.8%	0.3%
	Eurocode 3	1.37	15.6%	720	1.78	0.93	1.1%	81.3%	71.3%
	A.I.S.C.	0.95	16.9%	720	2.32	0.63	57.2%	10.1%	5.0%
$N + M_y + M_z$	O.I.C.	1.10	7.2%	1440	1.40	0.89	3.2%	47.1%	8.8%
	Eurocode 3	1.30	17.2%	1440	2.01	0.90	1.1%	81.6%	56.6%
	A.I.S.C.	0.93	16.3%	1440	1.84	0.64	67.7%	9.9%	4.2%

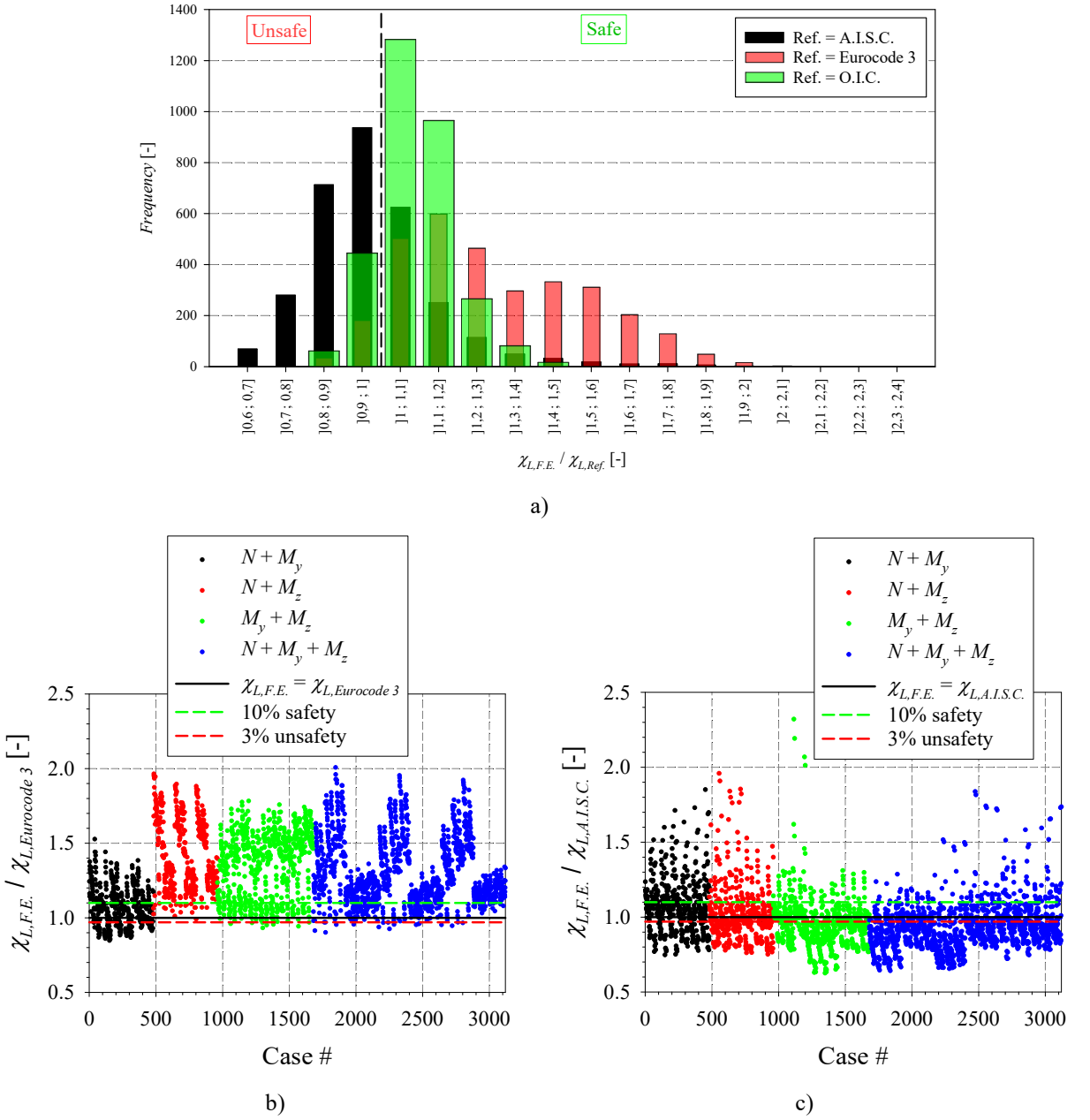

Figure 17: Performance of proposed approach vs existing ones (Eurocode 3 and A.I.S.C.) for combined load cases – a) Overall statistical summary – b) Results for Eurocode 3 – c) Results for A.I.S.C.

5. Conclusions

This paper relates to the behaviour and design of stainless steel open WF shapes. In a first step, the paper describes non-linear shell F.E. models and their validation against various sources of test data. Once confirmed adequate and accurate, the numerical models are used to collect a 3 000+ database of reference results that are used to assess the merits of a new O.I.C.-based design proposal. This original design method is based on a 2-stage approach for simple load cases, which relies on strain levels for compact sections and on an original cross-section relative slenderness λ_L for slender sections. Extension to combined load cases is based on the definition of a 3D resistance surface in the $N - M_y - M_z$ space and on the use of a system of spherical

coordinates. The proposed approach is shown to lead to very satisfactory resistance estimates, which are proved to be accurate, economic, safe and consistent. Compared to the existing design provisions for stainless steel in Eurocode 3 or in the A.I.S.C. recommendations, the proposed approach is seen to significantly improve design predictions so that it may be considered as an alternative design proposal for practitioners.

6. References

Abaqus (2011). "Abaqus 6.11:" *Dassault Systemes Simulia Corporation, Providence, RI, USA*.

Afshan, S. and Gardner, L. (2013). "The continuous strength method for structural stainless steel design:" *Thin-Walled Structures*, Vol. 68, pp. 42–49.

AISC (2013). AISC Design Guide 27 - Structural Stainless Steel, American Institute of Steel Construction, Chicago.

Ayrton, W.E. and Perry, J. (1886). "On struts:" *The Engineer*, Vol. 62.

Boissonnade, N., Hayeck, M., Saloumi, E. and Nseir, J. (2017). "An Overall Interaction Concept for an alternative approach to steel members design:" *Journal of Constructional Steel Research*, Vol. 135, pp. 199–212.

Bredenkamp, P.J., Van den Berg, G.J. and Van der Merwe, P. (1992). "Residual stresses and the strength of stainless steel I-section columns:" *Proc., Structural Stability Research Council, Annual Technical Session*, pp. 69–86.

Dawson, R.G. and Walker, A.C. (1972). "Post-buckling of geometrically imperfect plates:" *Journal of the Structural Division*,American Society of Civil Engineers Vol. 98, No. 1, pp. 75–94.

ECCS (1976). Manual on Stability of Steel Structures.

EN 1993-1-5 (2006). Eurocode 3: Design of Steel Structures: Part 1-5 – Plated structural elements, Brussels, Belgium.

EN 1993-1-4 (2006). Eurocode3: Design of steel structures – Part 1–4: General rules – Supplementary rules for stainless steels, European Committee for Standardization, Brussels.

FINELg (2011). "FINELg User's Manual": *V9.2. Greisch Info – Department ArGEnCo – ULg*.

Gagné, A.-S. (2022). *Design of stainless steel welded I-sections by means of the Overall Interaction Concept*, MSc Thesis, Université Laval, Québec, Canada.

Gagné, A.-S., Gérard, L. and Boissonnade, N. (2020). "Design of stainless steel cross-sections for simple load cases with the O.I.C.:" *Journal of Constructional Steel Research*, Vol. 168, p. 105936.

Gardner, L. (2002). *A new approach to structural stainless steel design*, (Ph.D. Thesis), Department of Civil and Environmental Engineering, Imperial College.

Gardner, L. (2008). "The continuous strength method:" *Proceedings of the Institution of Civil Engineers - Structures and Buildings*, Vol. 161, No. 3, pp. 127–133.

Gardner, L. (2019). "Stability and design of stainless steel structures – Review and outlook:" *Thin-Walled Structures*, Vol. 141, pp. 208–216.

Gardner, L. and Nethercot, D.A. (2004). "Numerical Modeling of Stainless Steel Structural Components—A Consistent Approach:" *Journal of Structural Engineering*, Vol. 130, No. 10, pp. 1586–1601.

Gardner, L., Saari, N. and Wang, F. (2010). "Comparative experimental study of hot-rolled and cold-formed rectangular hollow sections:" *Thin-Walled Structures*, Vol. 48, No. 7, pp. 495–507.

Gardner, L., Talja, A. and Baddoo, N.R. (2006). "Structural design of high-strength austenitic stainless steel:" *Thin-Walled Structures*, Vol. 44, No. 5, pp. 517–528.

Gardner, L. and Theofanous, M. (2008). "Discrete and continuous treatment of local buckling in stainless steel elements:" *Journal of Constructional Steel Research*, Vol. 64, No. 11, pp. 1207–1216.

Gérard, L., Li, L., Kettler, M. and Boissonnade, N. (2019). "Recommendations on the geometrical imperfections definition for the resistance of I-sections:" *Journal of Constructional Steel Research*, Vol. 162, p. 105716.

Gérard, L., Li, L., Kettler, M. and Boissonnade, N. (2021). "Steel I-sections resistance under compression or bending by the Overall Interaction Concept:" *Journal of Constructional Steel Research*, Vol. 182, p. 106644.

Hayeck, M., Nseir, J., Saloumi, E. and Boissonnade, N. (2018). "Experimental characterization of steel tubular beam-columns resistance by means of the Overall Interaction Concept:" *Thin-Walled Structures*, Vol. 128, pp. 92–107.

Johansson, B., Maquoi, R., Sedlacek, G., Müller, C. and Beg, D. (2007). "Commentary and worked examples to EN 1993-1-5 Plated Structural Elements:" *JRC scientific and technical reports*,\copyright European Communities.

Li, L. and Boissonnade, N. (2022). "Local/global coupled instabilities of slender I-sections under compression:" *Thin-Walled Structures*, Vol. 172, p. 108842.

Li, L. and Boissonnade, N. (2023). "Design of mono-symmetric I-sections under combined load cases by the Overall Interaction Concept:" *Thin-Walled Structures*, Vol. 182, p. 110280.

Li, L., Gérard, L., Langlois, S. and Boissonnade, N. (2022). "O.I.C.-based design of mono-symmetric I-sections under simple load cases:" *Thin-Walled Structures*, Vol. 174, p. 109134.

M. Ashraf (2006). *Structural Stainless Steel Design: Resistance Based on Deformation Capacity*, (PhD thesis), Imperial College.

Pavlovcic, L. (2005). *Shear Resistance of Longitudinally Stiffened Webs of Plated Girders*, (PhD thesis), University of Ljubljana.

Real, E. and Mirambell, E. (2005). "Flexural behaviour of stainless steel beams:" *Engineering Structures*, Vol. 27, No. 10, pp. 1465–1475.

Saliba, N. and Gardner, L. (2013). "Cross-section stability of lean duplex stainless steel welded I-sections:" *Journal of Constructional Steel Research*, Vol. 80, pp. 1–14.

Schafer, B.W. and Peköz, T. (1998). "Computational modeling of cold-formed steel: characterizing geometric imperfections and residual stresses:" *Journal of Constructional Steel Research*, Vol. 47, No. 3, pp. 193–210.

Sun, Y. and Zhao, O. (2019). "Material response and local stability of high-chromium stainless steel welded I-sections:" *Engineering Structures*, Vol. 178, pp. 212–226.

Theofanous, M. and Gardner, L. (2010). "Experimental and numerical studies of lean duplex stainless steel beams:" *Journal of Constructional Steel Research*, Vol. 66, No. 6, pp. 816–825.

Young, B. and Liu, Y. (2003). "Experimental Investigation of Cold-Formed Stainless Steel Columns:" *Journal of Structural Engineering*, Vol. 129, No. 2, pp. 169–176.

Young, B. and Lui, W.-M. (2005). "Behavior of Cold-Formed High Strength Stainless Steel Sections:" *Journal of Structural Engineering*, Vol. 131, No. 11, pp. 1738–1745.

Yuan, H.X., Wang, Y.Q., Shi, Y.J. and Gardner, L. (2014). "Stub column tests on stainless steel built-up sections:" *Thin-Walled Structures*, Vol. 83, pp. 103–114.